

## Article

# Aging Characteristics of Stationary Lithium-Ion Battery Systems with Serial and Parallel Cell Configurations

Mehmet C. Yagci , Thomas Feldmann, Elmar Bollin, Michael Schmidt  and Wolfgang G. Bessler 

Institute of Sustainable Energy Systems (INES), Offenburg University of Applied Sciences, Badstrasse 24, 77652 Offenburg, Germany; thomas.feldmann@velomanie.de (T.F.); bollin@hs-offenburg.de (E.B.); schmidt@hs-offenburg.de (M.S.); wolfgang.bessler@hs-offenburg.de (W.G.B.)

\* Correspondence: mehmet.yagci@hs-offenburg.de

**Abstract:** The significant market growth of stationary electrical energy storage systems both for private and commercial applications has raised the question of battery lifetime under practical operation conditions. Here, we present a study of two 8 kWh lithium-ion battery (LIB) systems, each equipped with 14 lithium iron phosphate/graphite (LFP) single cells in different cell configurations. One system was based on a standard configuration with cells connected in series, including a cell-balancing system and a 48 V inverter. The other system featured a novel configuration of two stacks with a parallel connection of seven cells each, no cell-balancing system, and a 4 V inverter. The two systems were operated as part of a microgrid both in continuous cycling mode between 30% and 100% state of charge, and in solar-storage mode with day–night cycling. The aging characteristics in terms of capacity loss and internal resistance change in the cells were determined by disassembling the systems for regular checkups and characterizing the individual cells under well-defined laboratory conditions. As a main result, the two systems showed cell-averaged capacity losses of 18.6% and 21.4% for the serial and parallel configurations, respectively, after 2.5 years of operation with 810 (serial operation) and 881 (parallel operation) cumulated equivalent full cycles. This is significantly higher than the aging of a reference single cell cycled under laboratory conditions at 20 °C, which showed a capacity loss of only 10% after 1000 continuous full cycles.

**Keywords:** stationary electrical energy storage; lithium-ion battery; lithium iron phosphate (LFP); aging characteristics; microgrid operation



**Citation:** Yagci, M.C.; Feldmann, T.; Bollin, E.; Schmidt, M.; Bessler, W.G. Aging Characteristics of Stationary Lithium-Ion Battery Systems with Serial and Parallel Cell Configurations. *Energies* **2022**, *15*, 3922. <https://doi.org/10.3390/en15113922>

Received: 2 May 2022  
Accepted: 21 May 2022  
Published: 26 May 2022

**Publisher's Note:** MDPI stays neutral with regard to jurisdictional claims in published maps and institutional affiliations.



**Copyright:** © 2022 by the authors. Licensee MDPI, Basel, Switzerland. This article is an open access article distributed under the terms and conditions of the Creative Commons Attribution (CC BY) license (<https://creativecommons.org/licenses/by/4.0/>).

## 1. Introduction

Lithium-ion batteries (LIB) are today the most important technology for stationary electricity storage. The success of LIB technology is owed to continuously decreasing cell prices and growing energy densities [1]. The market for stationary batteries can be roughly divided into home storage systems (up to 30 kWh energy capacity, typically used in combination with a rooftop photovoltaic system), industrial storage systems (30 kWh to 1 MWh), and large storage systems (over 1 MWh, typically used for grid services). The main growth market today is in photovoltaic home storage systems, with an installed energy capacity in Germany of ca. 930 MWh by the end of 2018 [2] and ca. 1500 MWh by the end of 2020 [3]. The capacity of industrial storage systems in Germany accumulated to 110 MWh, and that of large storage systems to 550 MWh by the end of 2020 [3]. The costs of stationary lithium-ion battery systems dropped by around 50% between 2013 and 2020 [4]. By 2040, stationary storage requirement is expected to rise to almost 3 TWh due to the rapid further increase of renewable energy sources [5].

Despite this economic success, one of the main technical challenges is the uncertain lifetime of LIBs. There is currently no field experience older than ten years, because this technology essentially did not exist before 2013. Published empirical studies are scarce and usually refer only to systems consisting of a single or a few cells representative of the

real energy storage system [6,7]. In the case of field data, studies are often concerned with the aging of electric vehicle batteries with relatively small single-cell capacity [8]. To our knowledge, empirical aging data of commercial LIBs in a full-scale commercial stationary storage system has not yet been presented in the literature.

In contrast to battery-level data, there have been many studies of aging and lifetime at the single-cell level using dedicated laboratory experiments [9–15]. Data are available for different cell types (chemistries and cell geometries) and cycling conditions (temperature, C-rate). The main conclusion that can be drawn from these studies is that aging is a highly complex and nonlinear phenomenon, depending strongly on operation conditions, mainly temperature, cycle depth, current rate, and resting times. The reader is referred to review articles [16–19] for further reading. Physicochemical models have been used to support the understanding of this behavior [20–22].

The goal of the present study is to investigate cell and battery aging under realistic but well-controlled operating conditions. Here and in the following, we distinguish between the *cell level* (single prismatic lithium-ion battery cell), the *battery level* (commercial battery systems consisting of multiple cells, inverters, housing, etc.), and the *microgrid level* (local grids with batteries, photovoltaic panels, controllable sinks and a grid connection). The present study combines all these three scales, therefore providing a comprehensive insight.

Within the battery, the type of connection of cells in serial and/or parallel arrangements is referred to as *cell configuration*. Both serial configurations and parallel configurations have individual properties, strengths and weaknesses. These are summarized in Table 1. The general tendency today is to use serial cell configurations to increase the voltage to a level well-suited for DC/AC inverters (for grid-coupled applications) or for high-voltage DC systems (i.e., battery-powered electric vehicles). In the case of serial cell configuration, cell-to-cell capacity variations can influence overall stack performance. The cell with lowest capacity and/or highest internal resistance (IR) can dominate the overall stack behavior by reaching end of charge or end of discharge cut-off voltage much earlier than the other cells. To avoid this problem, elaborate cell-balancing strategies are required, which add cost and complexity to the battery. Even then, the weakest cell is forced into deeper cycles than the other cells, therefore accelerating aging.

**Table 1.** Properties of serial and parallel cell configurations.

	<b>Serial Cell Configuration</b>	<b>Parallel Cell Configuration</b>
Voltage and current	High voltage, low current	Low voltage, high current
Advantages	Low ohmic losses, cheaper circuit components	Passive self-balancing, robust towards cell-to-cell variations
Disadvantages	Active balancing required, performance prone to single-cell failures	High ohmic losses, high-current components required

Parallel cell configuration has a key advantage in this regard: cell balancing occurs passively as electrical energy is transferred from cell to cell via the parallel connection. Therefore, this configuration is robust to cell-to-cell capacity variations, and there is no need for cell-balancing components. Furthermore, the weakest cell is not necessarily forced into deeper cycles than the other cells, therefore accelerating aging. As a result, it can be expected that cell cost can be reduced by enabling the use of cells of different batches and/or histories together. However, higher ohmic losses occur due to high current through all components (e.g., cables, connectors, sensors, switches), which may increase the overall material cost of the battery. Furthermore, additional safety devices may be needed to rule out possible risks that can be caused by high passive balancing currents between inhomogeneously charged cells.

In the present study, we compare the operation and aging characteristics of two different battery architectures, a standard architecture with 14s1p serial configuration using a single inverter, and a novel architecture with parallel configuration, consisting of two

1s7p strings with individual inverters. Section 2 describes the experimental methodology. Section 3 presents the results. A discussion with focus on battery architecture is provided in Section 4. Finally, conclusions are drawn in Section 5.

## 2. Experimental Methodology

We apply a combined experimental methodology on three levels: the single-cell level, the battery level, and the system (microgrid) level, the details of which are described in the following subsections.

### 2.1. Cell Level

Lithium-ion battery cells with a lithium iron phosphate (LFP) positive electrode and a graphite negative electrode are among the most used chemistries for stationary storage applications due to their high cyclic lifetime and higher safety, compared to chemistries such as nickel manganese cobalt oxide (NMC) [23,24]. Throughout the present experiments, 180 Ah commercial LFP/graphite prismatic LIB cells (Shenzhen Sinopoly Battery Co., Ltd., Shenzhen, China, model SP-LFP180AhA) were used. The operating voltage range and nominal voltage are given by the manufacturer as 2.8–3.8 V and 3.2 V, respectively. A detailed electrical, structural and chemical analysis of the single cells is given elsewhere [25]. According to the data sheet, the electrolyte consists of lithium hexafluorophosphate salt in ethylene carbonate (EC), dimethyl carbonate (DMC), diethyl carbonate (DEC) and ethyl acetate (EA) solvents. The current collectors are made of copper for the negative and aluminum for the positive electrode [25].

A total of 30 cells were received as a single shipment. All cells underwent an initial characterization under well-defined laboratory conditions, which consisted of capacity tests and internal resistance (IR) measurements (Basytec XCTS) performed at 20 °C ambient temperature (CTS T-40/200 LI climate chamber). Capacity measurements were performed at 0.25 C (45 A) current rate with constant-current (CC) constant-voltage (CV) charge (CV phase cut-off current 0.02 C, 3.6 A) and CC discharge. IR measurements were performed at each 10% state of charge (SOC) from 90% SOC to 10% SOC. These SOCs were set based on the measured real capacity of each individual cell. IR was measured by applying a lower 0.026 C (4.8 A) current pulse for 10 s during a 0.26 C (48 A) continuous CC discharge. From the voltage response, IR was calculated according to

$$IR_{\text{pulse}} = -\frac{V(t_1) - V(t_0)}{I(t_1) - I(t_0)} \quad (1)$$

by taking  $t_1 - t_0 = 3$  s. As part of this protocol, when the SOC reached 50% and before the IR measurement was carried out, an electrochemical impedance spectrum was recorded (results not shown).

Additionally, for all checkups we also determined the IR from the CC charge/discharge curves as

$$IR_{\text{CC}} = \frac{\bar{V}_{\text{chg}} - \bar{V}_{\text{dis}} - \Delta V_{\text{hys}}}{2 \cdot I} \quad (2)$$

where  $\bar{V}_{\text{chg}}$  is the average charge voltage between 10% and 90% SOC and  $\bar{V}_{\text{dis}}$  the average discharge voltage between 90% and 10% SOC. In this calculation we must consider the thermodynamic voltage hysteresis known from LFP [26], which we quantified experimentally for our cell to  $\Delta V_{\text{hys}} = 42.9$  mV.

After initial characterization, 28 selected cells were integrated into two commercial battery systems. The battery-level operation (next section) was interrupted in regular time intervals for single-cell checkups to monitor changes in cell parameters due to system operation. These checkups were carried out after disassembling the battery and performing capacity and IR measurements (Biologic VMP3, Basytec XCTS) under controlled laboratory conditions in the climate chambers set to 20 °C. These measurements were performed with

identical protocols as the initial characterization measurements. For this reason, the initial characterization measurements are termed as “Checkup 0”.

The two remaining cells were electrically characterized in detail, and the results were published [25]. To assess aging under laboratory conditions, they were then subjected to continuous cycling consisting of 0.83 C (150 A) CCCV charge (0.05 C cut-off current) and CC discharge at 20 °C ambient temperature in a climate chamber. One cell was opened after 897 cycles for internal structural and morphological characterization [25]. The other cell continued to be cycled for 5900 cycles.

## 2.2. Battery Level

Two commercial stationary energy storage battery systems (ASD Automatic Storage Device GmbH, Umkirch, Germany) with different battery architectures were used for battery-level tests. The two cell configurations are shown in Figure 1. Each battery has a total of 14 single cells packed closely inside the respective battery cabinets. A standard configuration, in the following referred to as *serial* battery architecture, is built by serial connection of 14 cells in 14s1p configuration, and operated by a single DC/AC inverter. A novel configuration, in the following referred to as *parallel* battery architecture, consists of two strings of seven parallel-connected cells in 1s7p configuration, each string operated by an individual DC/AC inverter. The serial configuration requires microelectronics for cell balancing, as visible in Figure 1a, while the parallel configuration does not. Here, the individual cell terminals are connected in parallel with current-collection rails made from copper. The two systems feature two different inverters. The serial system has a 48 V (DC)–220 V (AC) 2.4 kW inverter (Studer, Xtender XTM 2600-48). The parallel system features two 4 V (DC)–220 V (AC) inverters (ASD, Pacadu).

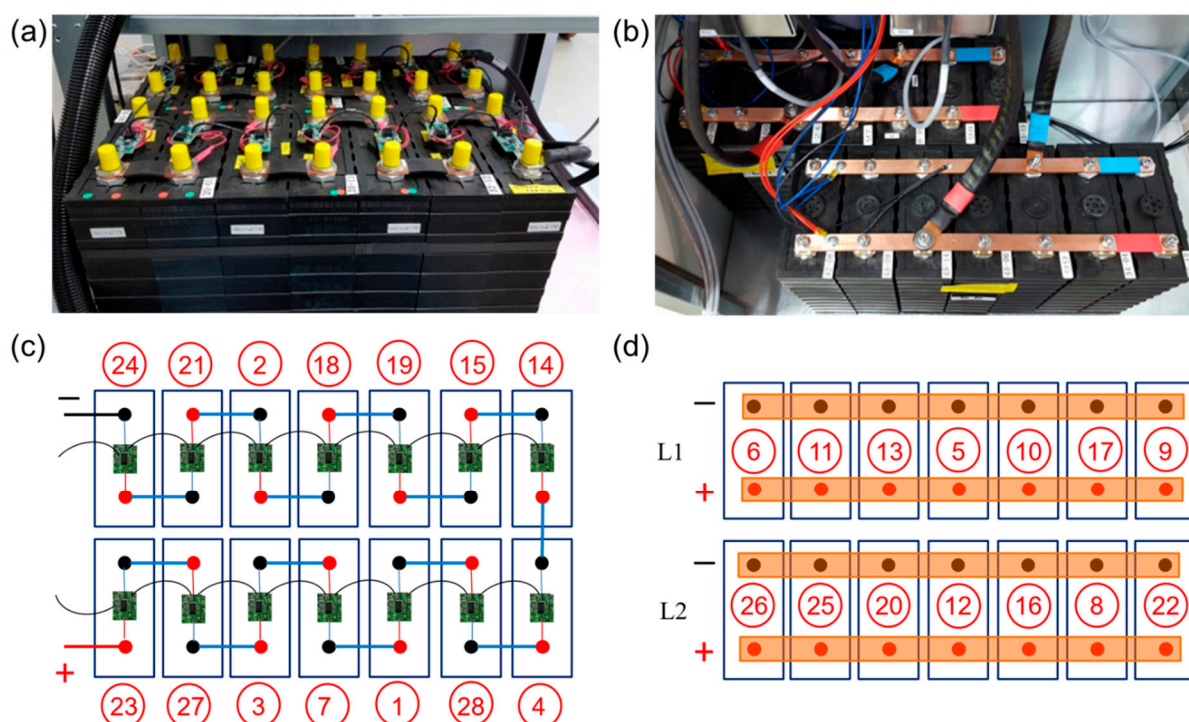


**Figure 1.** Photograph and schematic representation of the two different 14-cell battery architectures, (a,c) serial (one 14s1p stack) and (b,d) parallel (two 1s7p stacks L1 and L2 with individual inverters). The cell number is given as the integer values in the red circles.

The battery systems do not have a dedicated temperature control. There are no active cooling components or fans present in serial system cabinet. The cabinet of the parallel system has two fans (Sunon, DP200A, ca. 160 m<sup>3</sup>/h). Thus, the laboratory temperature has

a strong influence on the cell temperature. The microgrid laboratory, in turn, has no active cooling system and the room temperature is subject to strong seasonal fluctuations. For the present investigations, no additional active cooling systems were installed inside the battery systems or in the laboratory to keep the operating conditions close to real customer usage. The outside air temperature was measured by the weather station of Offenburg University of Applied Sciences mounted on the rooftop of a university building. For each cell stack, the temperature was measured using a temperature sensor (Pt 100) located between two cells.

The single cells were transferred between the battery systems and single-cell testing facilities described in the previous section by disassembling the systems, both for initial characterization and for a total of three checkups over almost three years.

### 2.3. Microgrid Level

The two battery systems, as delivered by the manufacturer, were integrated into a three-phase microgrid that was developed and set up at the Institute of Sustainable Energy Systems (INES) at Offenburg University of Applied Sciences (Offenburg, Germany) [27]. The setup is shown in Figure 2. The microgrid consists of a photovoltaic generator with 6.5 kW nominal power including three inverters (one for each phase, SMA, Sunny Boy 2000 HF, 2 kW), a small wind turbine (BRAUN Windturbinen GmbH, ANTARIS SW5.5 Generator CK 7.5, 4.5 kW), the two battery storage systems (as described above), three controllable loads (one per phase, Chroma Ate Inc., Taoyuan City, Taiwan, 63803 Programmable AC&DC Electronic Load, 3.6 kW), as well as the institute office tract and a battery electric vehicle as consumers. The microgrid can be operated both alone and in connection with the external grid. The central system components are three network managers (one for each phase, Studer XTM 4000-48) (Figure 2c), which can form an island network and include battery charging and inverter functionality. All components are fully controlled via a programmable logic controller (PLC) (Beckhoff, CX2040). To avoid possible interactions between the investigated battery systems and the inverters of the network managers, the batteries were placed outside the actual microgrid. However, the control and the operating modes were carried out as if they were parts of the microgrid.

For the present study, the two battery systems were operated strictly synchronously. The systems were controlled by the central PLC of the microgrid, which provided time-dependent AC power setpoints to the battery systems that were either given by the user or by an optimization algorithm (cf. below). The charge and discharge currents were continuously monitored and limited (depending on SOC) by the internal energy management of the battery systems. One goal of the present investigations was to study the influence of cell configuration on aging behavior. To obtain reliable results from the long-term cycling test, it had to be ensured that the cells in the two battery systems are subjected to identical loads. The different capacities of the battery systems, which were due to the deviations of the individual cell capacities from their nominal value as discussed in the next section, were compensated for by SOC-controlled charging and discharging, i.e., charging or discharging over a given SOC range in the same period of time. The difference in the AC power required for this was not only due to the difference in cell capacity, but also due to the different system efficiencies resulting from internal energy consumption of power electronics and control of the two systems.

The battery systems were run in two different operating modes. The first mode, referred to as *full-cycle mode*, was applied with the intention of provoking fast aging. The battery systems were operated in continuous charging (0.15 C) and discharging (0.25 C) between 30% SOC and 100% SOC. One charge–discharge cycle took around 8.5 h. Higher power and thus higher C rates were not possible due to restrictions of the power electronics of the battery systems. The power required during charge was taken from the external grid. The power released during discharge was dissipated by the electronic loads.

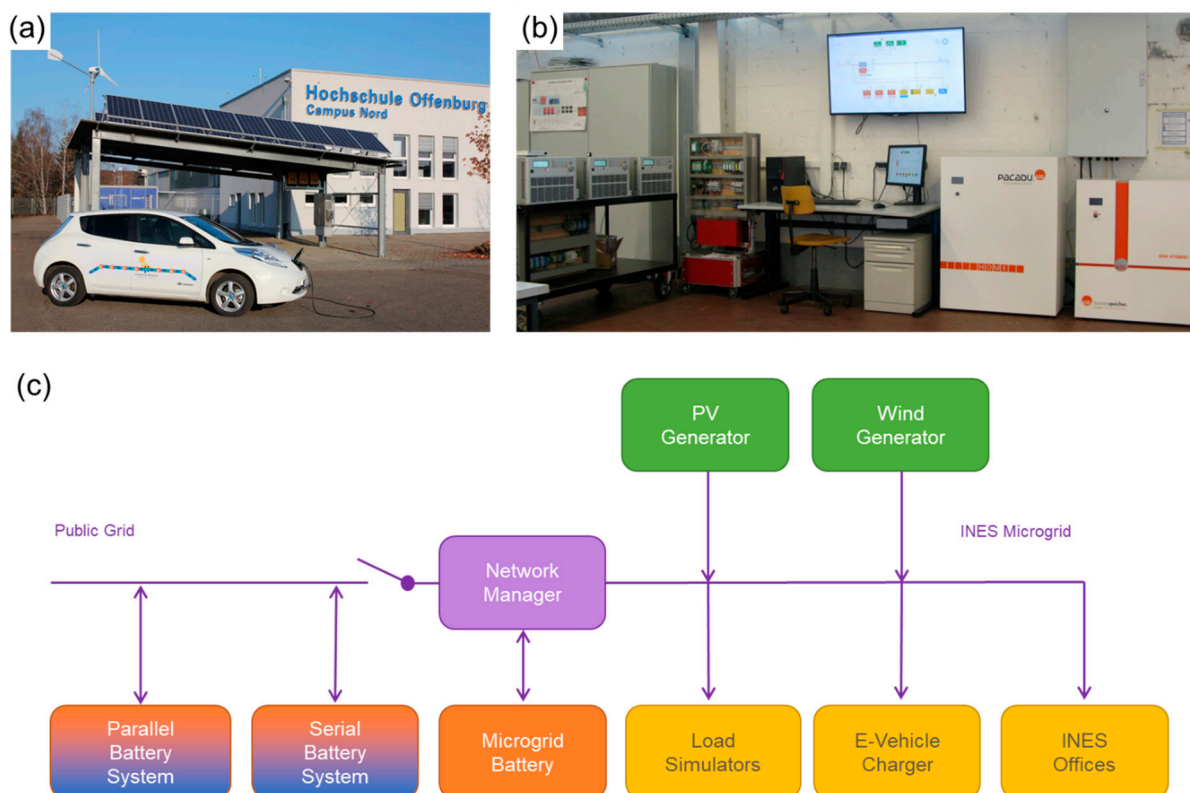


**Figure 2.** Microgrid at the Institute of Sustainable Energy Systems (INES) as operation base for the battery systems. (a) External view with wind and PV generators and battery electric vehicle, (b) internal view with serial and parallel battery systems (right), load simulators (left) and network control units (center), (c) operational scheme.

Additionally, for a period of 80 days, the systems were operated in a *solar-storage mode*, where the batteries were charged from the PV system during the day and discharged into the building during the night. Specifically, this mode was controlled by applying an optimization algorithm developed earlier [28,29]. In the present study, two optimization goals were combined: on the one hand, the reduction of load peaks when feeding and drawing energy into the public power grid, and on the other hand the prevention of cell states that are known to cause accelerated aging. The optimization algorithm was realized based on a model-predictive controller (MPC), which includes weather and load forecasts. The reader is referred to [29] for details. The resulting load profiles are qualitatively similar to what would be expected from a standard controller. It is, therefore, expected that the use of the MPC algorithm does not change the overall conclusions of the present work on battery aging.

### 3. Results

#### 3.1. Initial Cell Characterization and Selection

An initial characterization of the commercial cells was carried out to have a reference for the later measurements. The results of capacity and IR measurements of all 28 cells are shown in Figure 3. Panel (a) shows charge/discharge curves. Apart from very low and very high SOCs, the cells exhibit the flat voltage behavior typical for LFP-based cells. Most obvious, however, despite being nominally identical cells, measured capacities show a strong capacity variation, ranging from 158.8 to 195.7 Ah (18.9% capacity variation). Panel (b) shows the IR of the cells from pulse tests as a function of SOC. All cells show a slightly decreasing IR with increasing SOC, yet with a distinct peak at 50% SOC. We attribute this peak to the fact that, at 50% SOC, the pulse tests were interrupted to measure

electrochemical impedance spectra. Similar to individual cell capacities, there is a strong cell-to-cell IR variation. At 50% SOC, the values range from 0.59 to 0.98 m $\Omega$ .

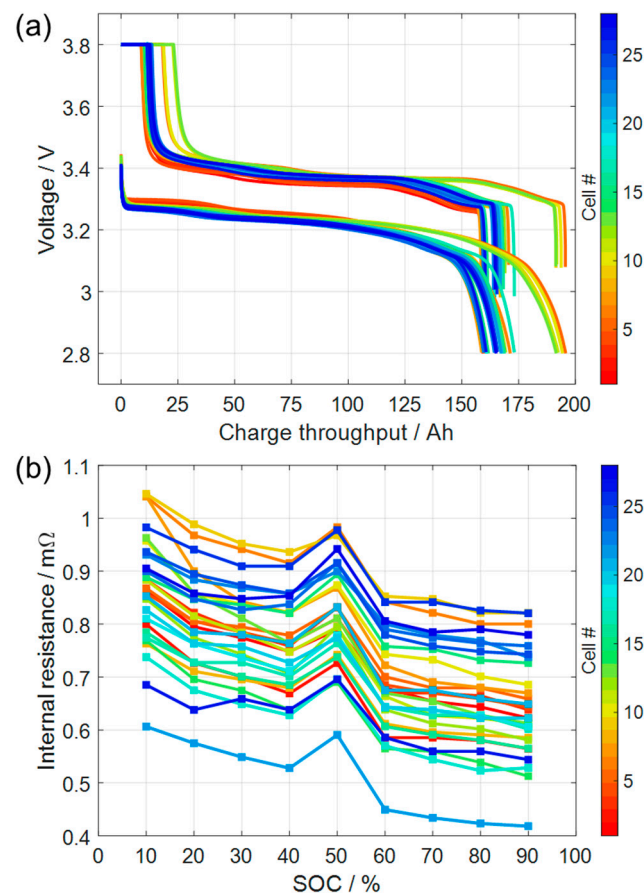


**Figure 3.** Initial characterization of 28 cells for use in the battery systems. (a) Galvanostatic cycling at 0.25 C. The lower branch on the curves represent discharge, where time progresses from left to right; the upper branch of the curves represent charge, where time progresses from right to left. (b) Internal resistance  $IR_{\text{pulse}}$  from 3 s pulse tests (see Equation (1)) as function of SOC.

These data are summarized in Figure 4 by plotting IR as function of capacity. The data show that there is no correlation between these two performance indicators. As summarized in Table 1 and discussed in the Introduction, cell-to-cell variations can be rather tolerated in a parallel cell configuration due to passive balancing, whereas capacity homogeneity is essential for the serial cell configurations to eliminate the influence of possible “weak” cells to exhibit overcharge/overdischarge. To test this hypothesis, for the serial system, 14 cells with minimum capacity and IR difference were selected. The remainder of the cells was allocated to the parallel system, as indicated in Figure 4. These cells were selected in such a way that the first stack (L1) consisted of cells with a high capacity variation and the second stack (L2) consisted of relatively low (<5 Ah) capacity variation. Furthermore, selection of cells with high capacity variation enabled the monitoring of the possible architectural advantage of the parallel system of being relatively insusceptible to cell inhomogeneity due to passive balancing currents via the parallel connection. A statistical analysis of the cell selection is given in Table 2. The standard deviation of the capacities in the serial system is 2.18 Ah, which is significantly lower than the value of 11.35 Ah for the parallel system. The standard deviations of the IR are 0.071 m $\Omega$  and 0.085 m $\Omega$  for the serial and parallel systems, respectively.

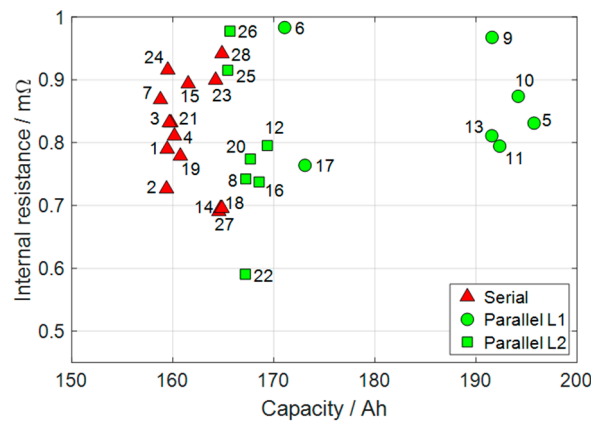


**Figure 4.** Initial internal resistance at 50% SOC as a function of initial cell capacity for all 28 cells, as well as distribution of the cells to the two battery systems.

**Table 2.** Statistical analysis of initial characterization tests of the two stack architectures.  $\Delta$  variation,  $\mu$  mean value,  $\sigma$  standard deviation.

	Capacity			Internal Resistance		
	$\Delta/\text{Ah}$	$\mu/\text{Ah}$	$\sigma/\text{Ah}$	$\Delta/\text{m}\Omega$	$\mu/\text{m}\Omega$	$\sigma/\text{m}\Omega$
Serial cell configuration	6.08	161.59	2.18	0.251	0.812	0.071
Parallel cell configuration	30.3	177.18	11.35	0.392	0.825	0.085

### 3.2. Microgrid Operation

After the single-cell initial checkup and selection as described above, the cells were assembled into the two battery systems. The systems were operated as part of the microgrid over an extended period of time (around 1000 days). The timeline of the experiments is shown in Figure 5. Panel (a) shows the cumulated equivalent full cycles (EFC) as a function of time, which we define as

$$\text{EFC} = \frac{\text{Total energy discharged}}{\text{Initial energy}} = \frac{\int P dt}{U_N \sum C_i} \quad (3)$$

where  $P$  is the discharge power,  $t$  the discharge time,  $C_i$  the initial discharge capacity of individual cell  $i$ ,  $U_N$  the nominal cell voltage, and the sum  $i$  runs over all cells in the battery. The type of operation mode is indicated in the plot within the respective timeframe, which was either full-cycle mode or solar-storage mode. Additionally, the periods of the checkups are indicated, where the systems were disassembled, the single cells individually characterized, and the systems reassembled. Minor rest phases during the operation periods were due to system and/or laboratory shutdowns. Over a total period of almost three years, the serial and parallel systems accumulated 810 and 881 EFCs, respectively. As the operating power was scaled to the individual system capacities as described in Section 2.3, both serial and parallel system exhibited a similar number of EFCs.

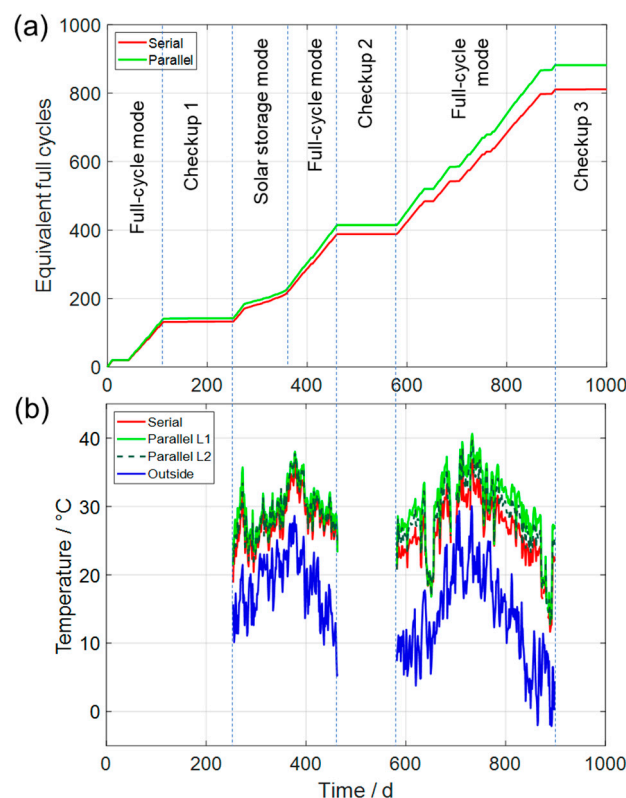


**Figure 5.** Timeline of the microgrid operation including rests for cell checkup experiments. (a) Accumulated equivalent full cycles for the two battery systems. (b) Daily average of measured temperatures.

Temperature is known to have a strong influence on cell aging [20]. Figure 5b shows measured cell and outside temperatures (daily averages) as a function of time. Temperature measurements were integrated into the test setup only after the first checkup, therefore the data are missing for the initial operation phase. Outside temperature shows a distinct seasonal variation, ranging between 5 and 30 °C. The temperatures inside the battery housings show a corresponding variation; however, they are up to 10 °C higher. The parallel system shows systematically higher temperatures than the serial system by ca. 2 °C. As mentioned earlier, the battery systems investigated here do not have dedicated cooling for battery stacks. As a result, the temperature difference between the two battery systems can be a result of higher currents and corresponding higher ohmic losses in the parallel system.

To allow a more detailed insight into battery operation, Figure 6 shows exemplary 48 h data of SOC, current and voltage for the two battery systems, both for solar-storage mode (left panels) and full-cycle mode (right panels). In solar-storage mode, the systems exhibit a day–night partial cycle, becoming fully charged during the day and then discharged down to around 50% SOC during the evening and night. In full-cycle mode, the systems are operated between 30% and 100% SOC as set by the microgrid controller. The current and voltage characteristics are representative of the two architectures: the serial system shows high voltages (around 46 V) and low currents (up to 35 A), while the parallel system shows low voltages (around 3.4 V, corresponding to the single-cell voltage) and high currents (up to 350 A).

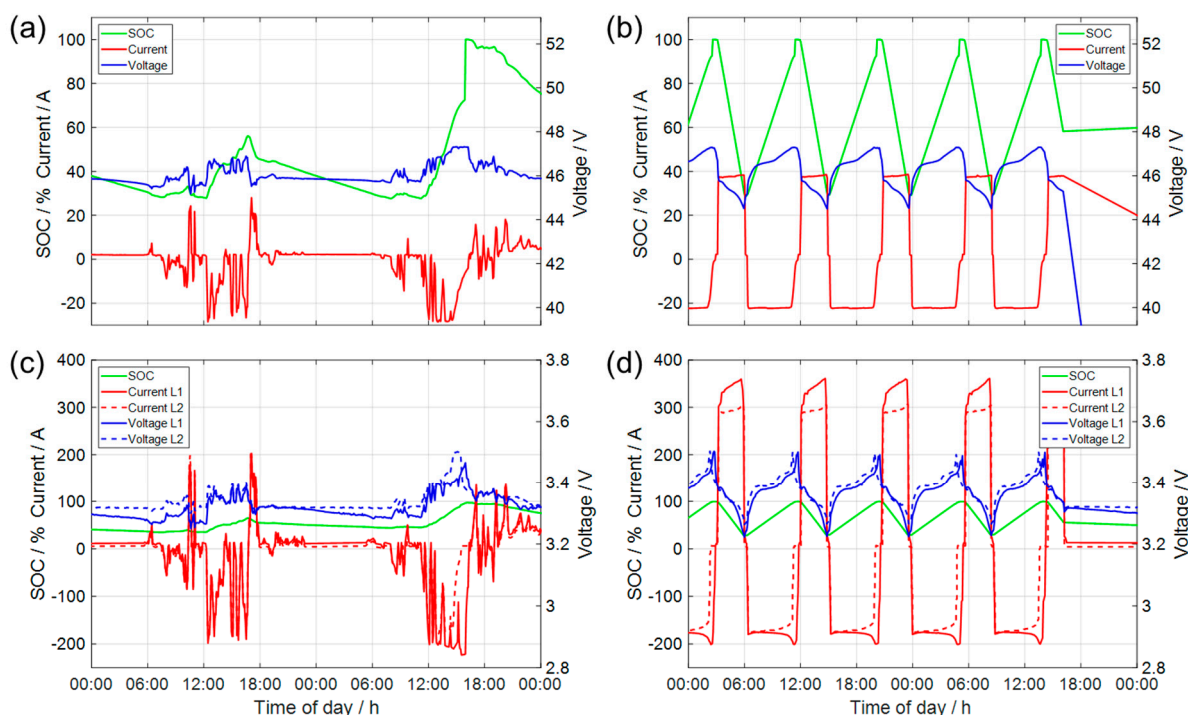


**Figure 6.** Exemplary operation data over 48 h time periods: SOC, current and voltage. (a) Serial system, solar-storage mode; (b) serial system, full-cycle mode; (c) parallel system, solar-storage mode; (d) parallel system, full-cycle mode. The scale ranges of the voltage axes correspond to the nominal voltage operation windows of the cells, respectively, and the system.

### 3.3. Comparison between Periodic Checkups

A total of three checkups were performed as indicated in Figure 5. The first checkup was performed after a 112-day period of full-cycle mode operation. The second checkup was performed after a mixed full-cycle mode and solar-storage mode operation of 210 days. The third checkup was performed after an extended 317 days full-cycle operation. As a result, the checkups were performed after 131, 388 and 810 (serial) and 141, 414 and 881 (parallel) equivalent full cycles, which correspond to 112, 462 and 897 days of testing, respectively. The checkup intervals are not constant because of the technical inflexibilities of assembling and disassembling battery storage systems into and from a running microgrid.

The evolution of the discharge/charge characteristics of four exemplary cells are shown in Figure 7. Each panel compares the performance during the three checkups as well as the initial performance (“Checkup 0”). For each system (serial shown on the left, parallel on the right), one cell with relatively low capacity loss and the cell with highest capacity loss are shown. A significant capacity loss is visible for all cells, i.e., the discharge curves end at lower charge throughput for later checkups. At the same time, the voltage spread between the charge and discharge branches remains relatively unaffected—in the plateau range between ca. 25 and ca. 125 Ah charge throughput, the discharge curves are lying more or less on top of each other. This indicates that the IR of the cells is not strongly affected by ongoing operation. The loss of cell capacity is also associated with a shortening and shifting of the characteristic voltage plateaus attributed to the stoichiometry range of the graphite anode [25].

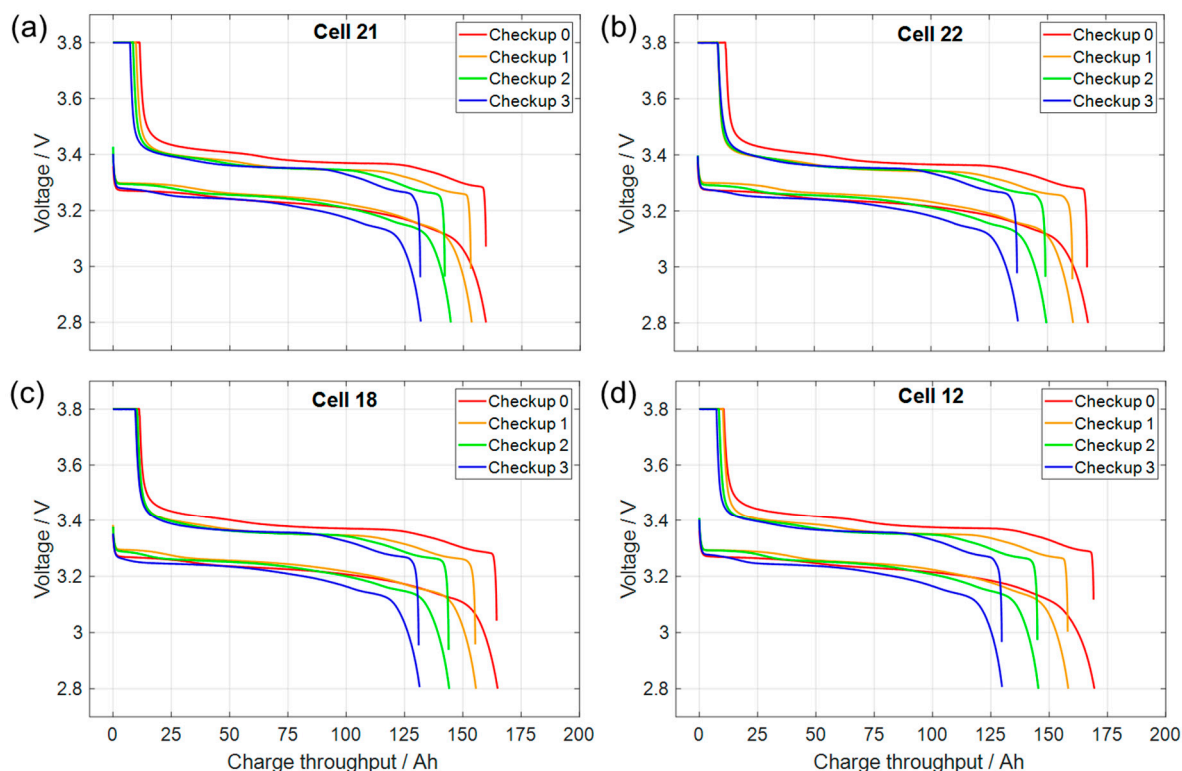


**Figure 7.** Charge/discharge behavior of exemplary individual cells with low capacity loss (a,b) and highest capacity loss (c,d) for serial (a,c) and parallel (b,d) battery architecture. “Checkup 0” corresponds to the initial characterization of the fresh cells.

As shown in Section 3.1, the cells show a wide distribution of initial capacity. Therefore, not only is the absolute capacity used for further analysis, but also the normalized capacity (i.e., capacity relative to initial capacity). Figure 8 shows the change in absolute and normalized capacities during the checkups as a function of cell number. The order of the cells in this figure corresponds to the arrangement in the stacks (Figure 1c,d). For all cells, capacity decreases monotonously with increasing cycling time, reaching around 80% of the initial capacity at Checkup 3. There is a clear cell-to-cell scatter. A statistical analysis of the capacity losses is given in Table 3. After Checkup 3, the average capacity losses of cells amount to 18.6% in the serial system and 21.4% in the parallel system. Additionally, the scatter is larger in the parallel system than in the serial system. Therefore, the cells in the parallel system have aged slightly more than those of the serial system. This will be further discussed in the next section.

**Table 3.** Capacity losses of serial and parallel system cells normalized to initial capacities.  $\Delta$  variation,  $\mu$  mean value,  $\sigma$  standard deviation.

	Serial			Parallel		
	$\Delta$ /%	$\mu$ /%	$\sigma$ /%	$\Delta$ /%	$\mu$ /%	$\sigma$ /%
Checkup 1	2.1	4.3	0.6	3.9	5.9	1.4
Checkup 2	3.1	10.9	0.9	3.7	12.7	1.2
Checkup 3	4.1	18.6	1.2	5.4	21.4	1.5

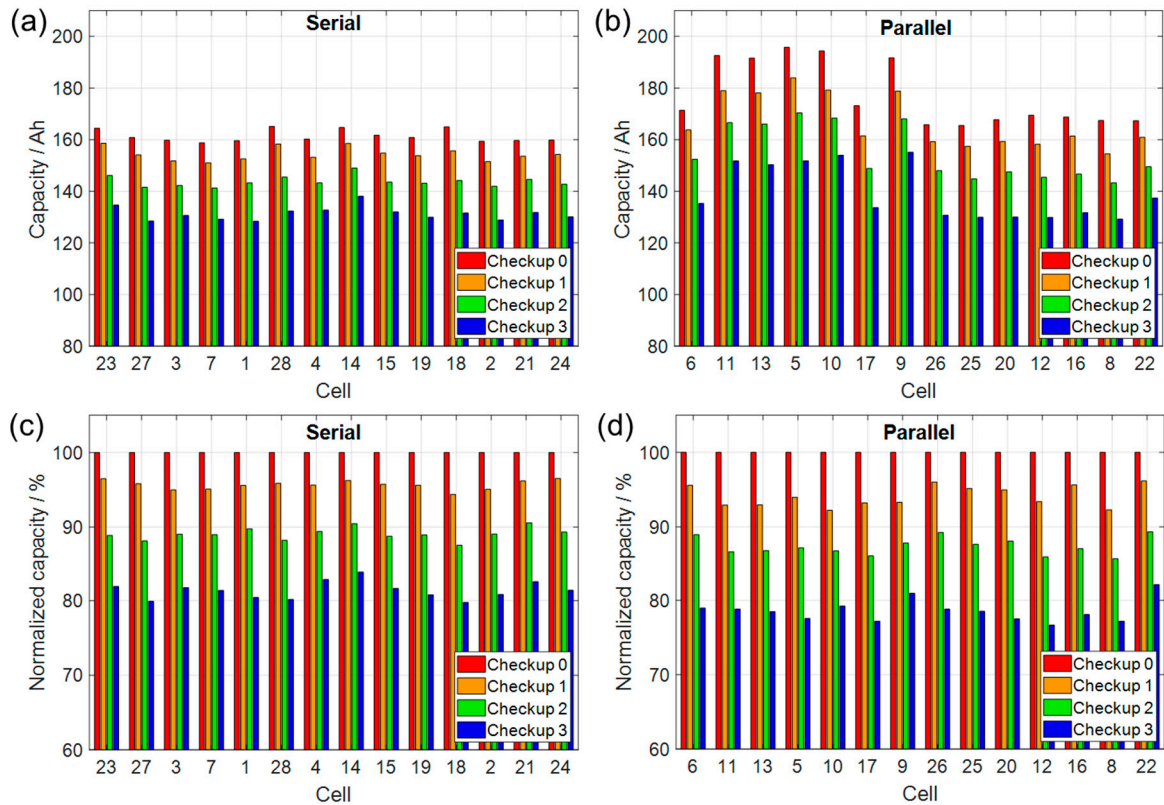


**Figure 8.** Absolute (a,b) and normalized (c,d) capacity for individual cells at each checkup.

### 3.4. Comparison between Initial and Final Checkups

In the previous section, we showed the capacity loss of the investigated 28 cells. To further analyze these findings, Figure 9 shows the influence of initial properties on the observed aging characteristics at the third checkup. Panel (a) shows capacity loss as a function of initial capacity. No clear trend of the data is observed within and between the two systems; only the slightly higher capacity losses in the parallel system are visible. Panel (b) shows capacity loss as a function of initial IR, again without clear trend. Panel (c) shows the change in IR as a function of initial capacity. This value was calculated as

$$\text{IR change} = \frac{\text{IR}_{\text{CC},3} - \text{IR}_{\text{CC},0}}{\text{IR}_{\text{CC},0}} \cdot 100 \% \quad (4)$$

We use the IR determined from the charge–discharge curves for this calculation (Equation (2)). These values are mostly negative (around  $-20\%$ ), meaning the IR decreased between initial and final checkups, although four cells showed IR increase. This will be further discussed below. Again, the plot shows no clear trend. Finally, panel (d) shows the IR change as a function of initial IR. The data for the cells in the serial system exhibit clear linear correlation: The magnitude of IR decrease is higher for the cells with higher initial IR. The reason for this behavior is unclear. It is connected to a large initial cell-to-cell scatter of  $\text{IR}_{\text{CC},0}$  between  $0.8\text{--}1.5 \text{ m}\Omega$ , while for the final checkup all cells converged towards similar values  $\text{IR}_{\text{CC},3}$  between  $1.05\text{--}1.2 \text{ m}\Omega$ .

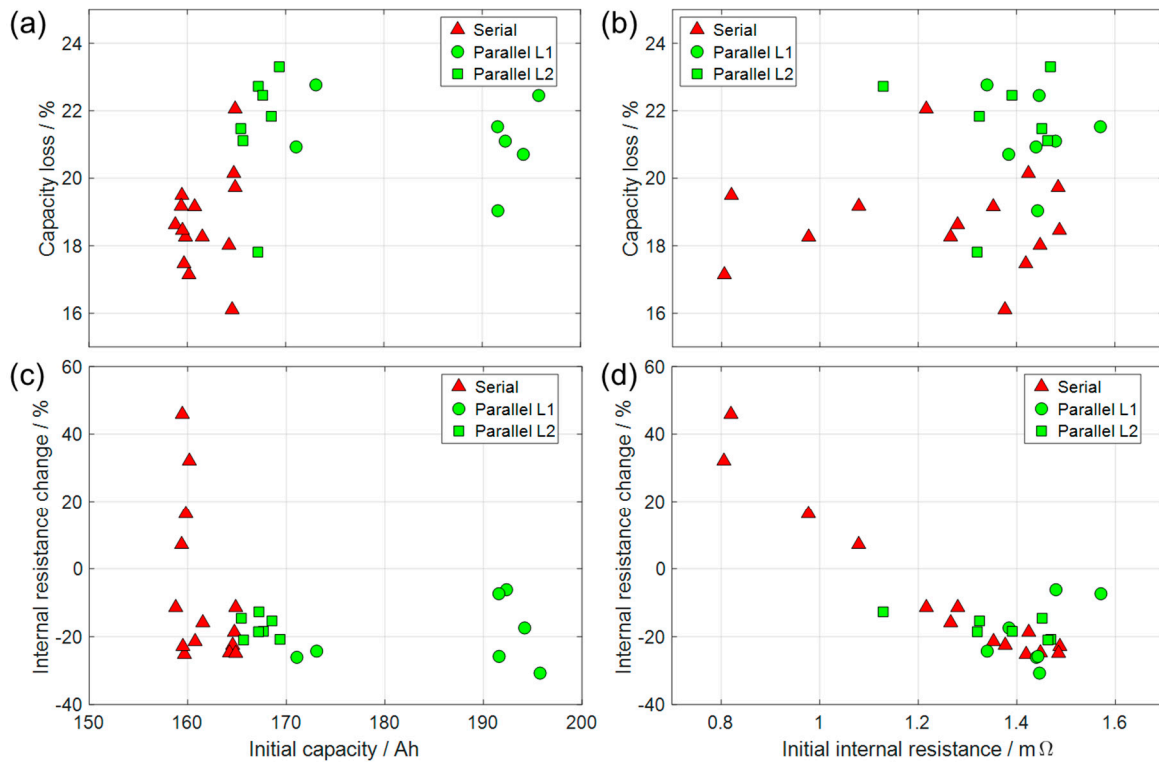


**Figure 9.** Capacity loss (a,b) and internal resistance change (c,d) at the end of microgrid operation depending on the initial capacity (a,c) and initial internal resistance (b,d).

3.5. Comparison to Single-Cell Cycling

For further assessment of aging behavior, an additional single cell from the same delivered batch was aged using continuous full cycles consisting of 0.83 C (150 A) CCCV charge and CC discharge at 20 °C ambient temperature in a climate chamber. This is the type of experiment typically used for assessing data-sheet behavior. Results are shown in Figure 10.

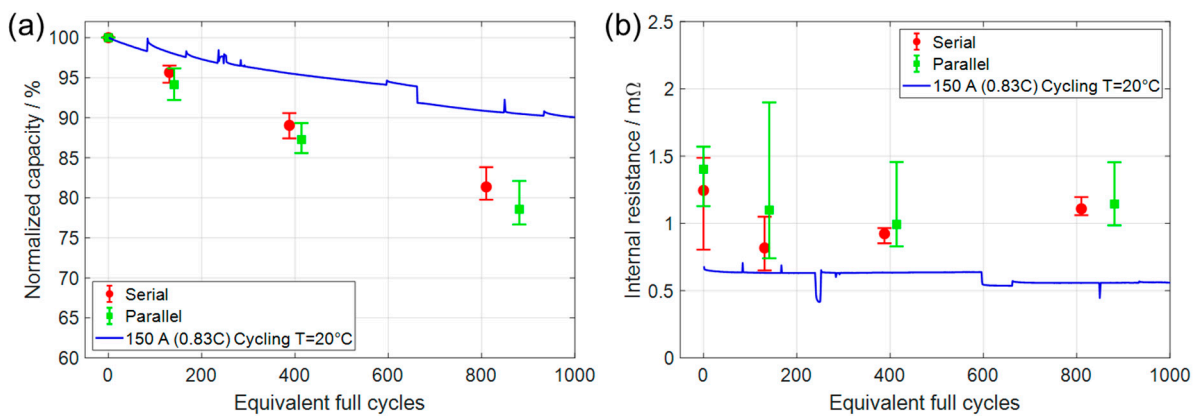


**Figure 10.** Comparison between the cells of the two battery systems (the error bars indicate the range of the 14 respective single cells) and an individual cell cycled with continuous full cycles. (a) Normalized capacity, (b) internal resistance calculated from the charge/discharge curves ( $IR_{CC}$ , see Equation (2)).

Figure 10a shows a comparison of the normalized capacity of this single cell and the average cell capacities of the two systems. The error bars indicate the range of the 14 respective single cells. The single cell exhibits a capacity loss of 10.0% after 1000 EFC.

Further cycling resulted in capacity losses of 20.3% after 3000 EFC and 34.3% after 4000 EFC (data not shown). This is better than the specifications given in the manufacturer's data-sheet, which claims < 20% capacity loss after 2000 cycles at 20 °C with C/3 currents.

It is interesting to compare these results to those of the capacity losses of the battery systems, plotted as points in Figure 10a. The comparison clearly shows that the single cycling cell exhibits a much smaller capacity loss than the system cells—the systems age about twice as fast as the single cell. These results are not only unexpected, but also highly problematic for system manufacturers who typically assign lifetime warranties based on single-cell testing results.

The IR of the additional single cell is plotted as a function of the cycle number in Figure 10b. Again, the data of the system cells are plotted as points and the range of the 16 cells as error bars. The single cell exhibits an essentially constant IR over the 1000 full cycles. The system cells show an IR drop from initial characterization (0 cycles) to the first checkup (ca. 135 cycles), and then an increase of IR until, at the last checkup, it has a similar value as initially. This means that the cells seem to have been activated during the first cycles, as already discussed above. The origin of the activation is unclear. The IR of the cycling cell is around a factor of two lower than that of the system cells. This might be due to a higher cell temperature resulting from the continuous 0.83 C cycling. It should be noted that the IR shows a strong cell-to-cell scatter (large error bars in Figure 10b). At present, it is not possible to assess if this is a real property of the cells or if this is caused by measurement inaccuracy (e.g., resulting from different contact resistances of the connection cables). For future studies, the IR measurement methodology of the quite low values (only around 1 mΩ) should be thoroughly validated.

#### 4. Discussion

In the previous sections, we presented the aging characteristics of a total of 28 cells operated in two battery systems with different cell configurations. The observed overall capacity loss of ca. 20% after ca. 2.5 years and ca. 850 EFC of operation is rather high for stationary applications, where lifetimes of >5000 EFC (corresponding to ca. 17 years of operation at 300 EFC per year [30]) are expected. Surprisingly, the single cell tested under laboratory conditions showed significantly lower capacity loss. Several potential reasons can be discussed as the origin of stronger aging of cells under system operation as opposed to cells under laboratory operation: (i) the influence of checkup experiments, (ii) the influence of current rate and cycling depth, (iii) the influence of inverters, (iv) the influence of cell balancing, (v) the influence of temperature. We believe that the influence of checkup tests can be neglected, as each checkup contributed only three full cycles to the total of 810 (serial) and 881 (parallel) equivalent full cycles.

Both a high cycling depth (depth of discharge, DOD) and high currents have been observed to accelerate capacity loss in lithium-ion battery cells [9,10,12]. During microgrid operation, the system cells undergo 70% depth of discharge (DOD) between 100% and 30% SOC during full-cycle mode. In the serial system, throughout full-cycle mode the maximum current is lower than 0.25C (45 A), on average 0.12C (22.1 A) at charge and 0.21C (38.5 A) at discharge. In the parallel system, single-cell currents are not measured separately but, for the sake of comparison, maximum charge and discharge currents can be assumed to be distributed equally to each cell. The maximum charge and discharge currents are calculated as a result of this assumption as 0.16 C (28.6 A) and 0.28 C (51.1 A), respectively. The single cycling cell, on the other hand, was subjected to full cycles (100% DOD) at much higher current (150 A). Therefore, the cycling conditions in the system are significantly softer than those for the single cell. This is opposite to the observation shown in Figure 10 and therefore cannot explain the difference.

Power electronics, in particular DC–AC inverters, are essential for the integration of stationary storage systems into the AC grid. During inverter operation, the batteries are subjected to fast (typically, 50 Hz) voltage fluctuations, referred to as ripples. These ripples result from incomplete suppression of high-frequency AC harmonics during AC–DC

rectification or from electrical noise generated by internal electronic switching operations of the power electronics [31]. Research performed on various lithium-ion battery types and different waveforms has demonstrated that there is not enough evidence to prove that ripples have an effect on lithium-ion battery aging [32–35]. It has been suggested that the electrochemical double-layer capacitance acts as a filter against AC harmonics, thus limiting their effect on cell aging [33,35]. On the other hand, it was recently shown that low-frequency harmonics below the corner frequency of the double-layer capacitance causes accelerated aging on NMC cells [36]. As a result, the effect of the inverters on the aging of the cells under investigation should be further investigated. This is, however, beyond the scope of the present study.

In the serial system, the cells had individual balancing circuits. These circuits induce additional currents and/or microcycles on the cells. The influence of these currents on aging has not been investigated so far, to the best of our knowledge. The parallel system does not have a balancing system; still, it can be expected that passive balancing currents occur between the cells during rest phases, corresponding to additional microcycles. The magnitude of the active or passive balancing currents is expected to be much smaller than the absolute charge and discharge currents. It is, therefore, unlikely that they are at the origin of the strong aging of the systems. Moreover, in the case of parallel configuration, the magnitude of passive balancing currents is expected to be higher in outlier cells, i.e., cells with highest and lowest capacities. However, the comparison of the capacity loss of cells depending on their initial capacities (Figure 9a) does not show accelerated aging of outlier cells.

The influence of temperature on cell aging has been observed in several studies of LFP cells [10,11,37–39]. The cylindrical 2.3 Ah cells investigated by Omar et al. showed ca. 15% decreased cycle life when increasing ambient temperature from 25 °C to 40 °C [10]. In calendaric aging tests of cylindrical 2.3 Ah cells by Sarasketa-Zabal et al., capacity decreased almost three times as fast at 50 °C compared to 30 °C [11]. Grolleau et al. investigated calendaric aging of 15 Ah cells and measured around 50% capacity loss after 450 days at 60 °C, compared to less than 5% capacity loss at 30 °C [38]. Safari and Delacourt measured 38% capacity loss of a 2.3 Ah cylindrical cell under cyclic aging at 45 °C, compared to only 11% at 25 °C [37]. Therefore, it is well established from previous studies that the higher the temperature, the faster the capacity loss. As already shown and discussed above (Figure 5), the temperatures in the systems show a significant seasonal variation. Additionally, the system cells are closely packed (Figure 1), which hinders heat transfer out of the cells. As consequence, measured cell-surface temperatures are quite high (up to 40 °C in summer) with strong temporal variation. The single cell was operated at constant 20 °C ambient temperature under strong convection in the climate chamber, and surface temperatures measured by a thermocouple during cycling were constant at 25 °C. Grolleau et al. give a thermal activation energy of 52.1 kJ/mol for the SOC-independent term of their aging model [38]. Kupper et al. used a thermal activation energy of 55.5 kJ/mol for the aging reaction implemented in their model [20]. Using a value of 53 kJ/mol, the Arrhenius equation yields a factor of two when increasing temperature from 25 °C (assumed single-cell temperature) to 35 °C (assumed average system-cell temperature). This agrees very well with the observations shown in Figure 10.

From this discussion, we tentatively conclude that the observed faster capacity loss of the cells operated in the system, as compared to the single-cell cycling experiment, is due to a difference in cell temperatures.

The temperature of individual cells in a battery system depends on the position within the stack. According to the discussion above, this should also affect aging behavior. The capacity losses as a function of the spatial position of the cells is shown in Figure 11. Indeed, the cells with the lowest capacity loss, in both battery architectures, are the ones at the sides of the stacks where convective heat losses to the ambient atmosphere is possible. Otherwise, for the serial system, there is no clear dependence of aging on cell position. For the parallel system, however, the strongest aging occurs towards the center of the two stacks. This

might be associated with the position of the main cables, which are located close to the center of the current collector rails (Figure 1). Therefore, the rails show the highest currents towards the stack center, which may be associated with highest ohmic heating (which is proportional to current squared) of the rails, higher temperatures of the cells in the center, and therefore stronger aging. The results thus show that the spatial position of cells within the stack does have a clear, albeit weak, influence on aging, and underline the need for a homogeneous thermal design of the battery system. Please note that we did not measure the actual temperature distribution of the stacks.

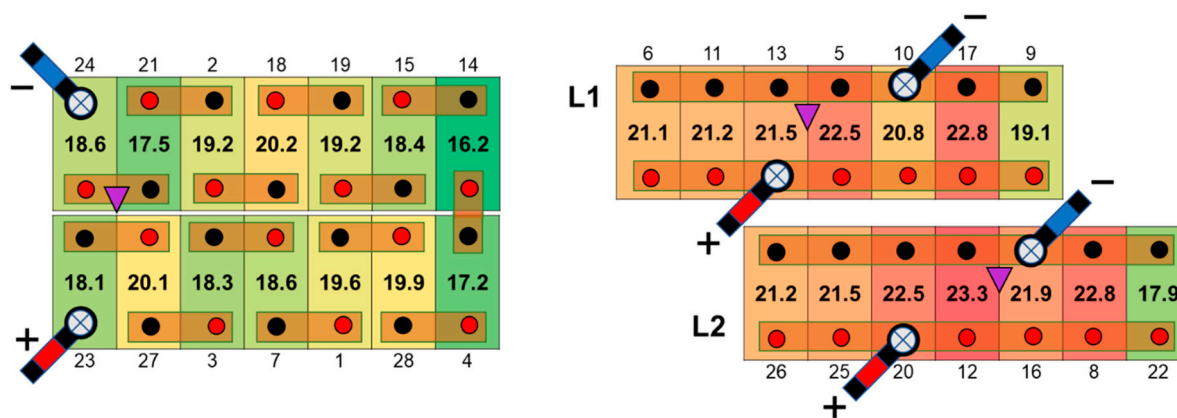


**Figure 11.** Capacity loss of the individual cells (given as numerical values in percent and as color code) of the two battery architectures (**left**: serial, **right**: parallel) according to the spatial position (Figure 1). The cell number is given in smaller font below the cells. The purple symbols indicate the position of the thermocouples used for recording the temperature data shown in Figure 5.

Assessing the difference in aging between serial and parallel cell configurations was an overall goal of the present investigation. Therefore, the two battery systems were operated strictly synchronously and under same ambient temperature conditions. As a consequence of the different system designs, this still resulted in different current loads and temperatures for the individual battery cells. Still, the difference between average capacity loss of two systems at the end of experiment was only 2.8%, which is within the capacity loss variation of the cells of both systems. We therefore conclude that, despite minor differences, there is no dominant configuration-specific influence on cell aging. The slightly higher capacity losses of the cells in the parallel system are probably due to higher temperature of the cells, as already discussed above. This possibly results from ohmic heating of the current-collection rails and the connection cables. Furthermore, the large initial cell-to-cell capacity variation of up to 30.3 Ah can lead to passive balancing currents between the cells during rest phases, which may cause additional microcycles and additional heat losses.

## 5. Conclusions

An experimental methodology for quantifying the aging characteristics of full-scale 8 kWh commercial stationary battery storage systems was designed and implemented. It consisted of investigation and operation at cell level, battery level, and microgrid level. Specifically, two different battery architectures were compared, one with serially connected cells and one with cells connected in parallel. The battery systems were operated over an extended period of time (ca. 2.5 years, ca. 850 equivalent full cycles). Single-cell characteristics were quantified initially and during periodic checkups. The key results of the investigations are:

- All cells show significant and continuous capacity loss. The average capacity loss after 2.5 years of battery operation was 18.6% and 21.4% for cells in the serial and parallel configuration, respectively. At the same time, the cells showed a decrease of internal resistance.

- A single cell operated with continuous full cycles showed significantly less (a factor of two) capacity loss than the cells in the system. The difference is probably caused by the higher temperature of the cells in the system, compared to the cells in the climate chamber. Therefore, improving thermal management at battery level (e.g., by integrating active cooling strategies) can probably significantly improve cell lifetime.
- The difference in aging between the serial and parallel battery architectures is only small and likely due to the higher and presumably more inhomogeneously distributed cell temperatures in the system with parallel architecture. Higher temperatures may result from higher ohmic losses in the current-collection rails due to significantly higher currents as compared to the serial architecture.

Considering that the parallel system was built up by individual cells with large initial capacity variation, this architecture has a promising economic advantage that enables the use of cells of different production batches or different stages of health to be used together in the same battery stack. Finally, the results presented in this manuscript demonstrate that the effect of cell temperature on aging is very important. Therefore, we suggest that an effective and preferably active cooling of the battery cells is a relatively low-cost, high-benefit measure to increase battery lifetime.

**Author Contributions:** Conceptualization, M.C.Y. and W.G.B.; software, M.C.Y. and T.F.; validation, M.C.Y.; formal analysis, M.C.Y.; investigation, M.C.Y. and T.F.; writing—original draft preparation, M.C.Y. and T.F.; writing—review and editing, W.G.B. and M.S.; visualization, M.C.Y. and T.F.; supervision, W.G.B., E.B. and M.S.; project administration, W.G.B., E.B. and M.S.; funding acquisition, W.G.B. and E.B. All authors have read and agreed to the published version of the manuscript.

**Funding:** This work was funded by the German Ministry of Education and Research (BMBF) in the framework of the STABIL project (grant no. 03FH004PX5). Single-cell experiments were partially carried out in the Enerlab 4.0 laboratory which was funded by the BMBF (grant no. 13FH091IN6).

**Acknowledgments:** The authors thank Michael Wirwitzki (Offenburg University of Applied Sciences) for supporting the microgrid integration and operation, and René Behmann (Offenburg University of Applied Sciences) for supporting cell characterization. The support of ASD Automatic Storage Device GmbH, Umkirch, Germany is gratefully acknowledged.

**Conflicts of Interest:** The authors declare no conflict of interest.

## References

1. Ziegler, M.S.; Trancik, J.E. Re-examining rates of lithium-ion battery technology improvement and cost decline. *Energy Environ. Sci.* **2021**, *14*, 1635–1651. [[CrossRef](#)]
2. Figgenger, J.; Stenzel, P.; Kairies, K.-P.; Linßen, J.; Haberschusz, D.; Wessels, O.; Angenendt, G.; Robinius, M.; Stolten, D.; Sauer, D.U. The development of stationary battery storage systems in Germany—A market review. *J. Energy Storage* **2020**, *29*, 101153. [[CrossRef](#)]
3. Stenzel, P.; Kotzur, L.; Stolten, D.; Figgenger, J.; Haberschusz, D.; Sauer, D.U.; Gottke, V.; Valentin, F.; Velten, A.; Schäfer, F.; et al. Energiespeicher. *BWK-Das Energ.-Fachmag.* **2021**, *73*, 20–34.
4. Haas, R.; Kemfert, C.; Auer, H.; Ajanovic, A.; Sayer, M.; Hiesl, A. On the economics of storage for electricity: Current state and future market design prospects. *WIREs Energy Environ.* **2022**, e431. [[CrossRef](#)]
5. Kebede, A.A.; Kalogiannis, T.; van Mierlo, J.; Bercibar, M. A comprehensive review of stationary energy storage devices for large scale renewable energy sources grid integration. *Renew. Sustain. Energy Rev.* **2022**, *159*, 112213. [[CrossRef](#)]
6. Bercibar, M.; Garmendia, M.; Gandiaga, I.; Crego, J.; Villarreal, I. State of health estimation algorithm of LiFePO<sub>4</sub> battery packs based on differential voltage curves for battery management system application. *Energy* **2016**, *103*, 784–796. [[CrossRef](#)]
7. Mingant, R.; Bernard, J.; Sauvart-Moynot, V. Novel state-of-health diagnostic method for Li-ion battery in service. *Appl. Energy* **2016**, *183*, 390–398. [[CrossRef](#)]
8. Schuster, S.F.; Brand, M.J.; Berg, P.; Gleissenberger, M.; Jossen, A. Lithium-ion cell-to-cell variation during battery electric vehicle operation. *J. Power Source* **2015**, *297*, 242–251. [[CrossRef](#)]
9. Ecker, M.; Nieto, N.; Käbitz, S.; Schmalstieg, J.; Blanke, H.; Warnecke, A.; Sauer, D.U. Calendar and cycle life study of Li(NiMnCo)O<sub>2</sub>-based 18650 lithium-ion batteries. *J. Power Source* **2014**, *248*, 839–851. [[CrossRef](#)]
10. Omar, N.; Monem, M.A.; Firouz, Y.; Salminen, J.; Smekens, J.; Hegazy, O.; Gaulous, H.; Mulder, G.; Van den Bossche, P.; Coosemans, T.; et al. Lithium iron phosphate based battery—Assessment of the aging parameters and development of cycle life model. *Appl. Energy* **2014**, *113*, 1575–1585. [[CrossRef](#)]

11. Sarasketa-Zabala, E.; Gandiaga, I.; Rodriguez-Martinez, L.M.; Villarreal, I. Calendar ageing analysis of a LiFePO<sub>4</sub>/graphite cell with dynamic model validations: Towards realistic lifetime predictions. *J. Power Source* **2014**, *272*, 45–57. [[CrossRef](#)]
12. Wang, J.; Liu, P.; Hicks-Garner, J.; Sherman, E.; Soukiazian, S.; Verbrugge, M.; Tataria, H.; Musser, J.; Finamore, P. Cycle-life model for graphite-LiFePO<sub>4</sub> cells. *J. Power Source* **2011**, *196*, 3942–3948. [[CrossRef](#)]
13. Fu, R.; Choe, S.-Y.; Agubra, V.; Fergus, J. Development of a physics-based degradation model for lithium ion polymer batteries considering side reactions. *J. Power Source* **2015**, *278*, 506–521. [[CrossRef](#)]
14. Watanabe, S.; Kinoshita, M.; Nakura, K. Capacity fade of LiNi<sub>(1-x-y)</sub>Co<sub>x</sub>Al<sub>y</sub>O<sub>2</sub> cathode for lithium-ion batteries during accelerated calendar and cycle life test. I. Comparison analysis between LiNi<sub>(1-x-y)</sub>Co<sub>x</sub>Al<sub>y</sub>O<sub>2</sub> and LiCoO<sub>2</sub> cathodes in cylindrical lithium-ion cells during long term storage test. *J. Power Source* **2014**, *247*, 412–422. [[CrossRef](#)]
15. Leonardi, S.G.; Aloisio, D.; Brunaccini, G.; Stassi, A.; Ferraro, M.; Antonucci, V.; Sergi, F. Investigation on the ageing mechanism for a lithium-ion cell under accelerated tests: The case of primary frequency regulation service. *J. Energy Storage* **2021**, *41*, 102904. [[CrossRef](#)]
16. Abraham, D.P.; Reynolds, E.M.; Sammann, E.; Jansen, A.N.; Dees, D.W. Aging characteristics of high-power lithium-ion cells with LiNi<sub>0.8</sub>Co<sub>0.15</sub>Al<sub>0.05</sub>O<sub>2</sub> and Li<sub>4/3</sub>Ti<sub>5/3</sub>O<sub>4</sub> electrodes. *Electrochimica Acta* **2005**, *51*, 502–510. [[CrossRef](#)]
17. Palacín, M.R. Understanding ageing in Li-ion batteries: A chemical issue. *Chem. Soc. Rev.* **2018**, *47*, 4924–4933. [[CrossRef](#)]
18. Vetter, J.; Novák, P.; Wagner, M.R.; Veit, C.; Möller, K.-C.; Besenhard, J.O.; Winter, M.; Wohlfahrt-Mehrens, M.; Vogler, C.; Hammouche, A. Ageing mechanisms in lithium-ion batteries. *J. Power Source* **2005**, *147*, 269–281. [[CrossRef](#)]
19. Alipour, M.; Ziebert, C.; Conte, F.V.; Kizilel, R. A Review on Temperature-Dependent Electrochemical Properties, Aging, and Performance of Lithium-Ion Cells. *Batteries* **2020**, *6*, 35. [[CrossRef](#)]
20. Kupper, C.; Weißhar, B.; Reißmann, S.; Bessler, W.G. End-of-Life Prediction of a Lithium-Ion Battery Cell Based on Mechanistic Aging Models of the Graphite Electrode. *J. Electrochem. Soc.* **2018**, *165*, A3468–A3480. [[CrossRef](#)]
21. Carelli, S.; Bessler, W.G. Prediction of reversible lithium plating with a pseudo-3D lithium-ion battery model. *J. Electrochem. Soc.* **2020**, *167*, 100515. [[CrossRef](#)]
22. Reniers, J.M.; Mulder, G.; Howey, D.A. Review and Performance Comparison of Mechanical-Chemical Degradation Models for Lithium-Ion Batteries. *J. Electrochem. Soc.* **2019**, *166*, A3189–A3200. [[CrossRef](#)]
23. Zhang, W.-J. Structure and performance of LiFePO<sub>4</sub> cathode materials: A review. *J. Power Source* **2011**, *196*, 2962–2970. [[CrossRef](#)]
24. Li, Z.; Zhang, D.; Yang, F. Developments of lithium-ion batteries and challenges of LiFePO<sub>4</sub> as one promising cathode material. *J. Mater. Sci.* **2009**, *44*, 2435–2443. [[CrossRef](#)]
25. Yagci, M.C.; Behmann, R.; Daubert, V.; Braun, J.A.; Velten, D.; Bessler, W.G. Electrical and Structural Characterization of Large-Format Lithium Iron Phosphate Cells Used in Home-Storage Systems. *Energy Technol.* **2021**, *9*, 2000911. [[CrossRef](#)]
26. Dreyer, W.; Jamnik, J.; Guhlke, C.; Huth, R.; Moškon, J.; Gaberšček, M. The thermodynamic origin of hysteresis in insertion batteries. *Nat. Mater.* **2010**, *9*, 448–453. [[CrossRef](#)] [[PubMed](#)]
27. Dongol, D.; Feldmann, T.; Schmidt, M.; Bollin, E. A MPC Based Peak Shaving Application for a Household with Photovoltaic Battery System. In *Smart Cities, Green Technologies and Intelligent Transport Systems, Proceedings of the SMARTGREENS 2018, VEHITS 2018 Communications in Computer and Information Science, Funchal, Madeira, Portugal, 16–18 March 2019*; Springer: Berlin/Heidelberg, Germany, 2019; Volume 992, pp. 44–66. [[CrossRef](#)]
28. Dongol, D.; Feldmann, T.; Bollin, E. An Overview to the concept of Smart Coupling and Battery Management for Grid connected Photovoltaic System. *J. Electron. Sci. Technol.* **2015**, *13*, 367–372. [[CrossRef](#)]
29. Dongol, D.; Feldmann, T.; Schmidt, M.; Bollin, E. A model predictive control based peak shaving application of battery for a household with photovoltaic system in a rural distribution grid. *Sustain. Energy Grids Netw.* **2018**, *16*, 1–13. [[CrossRef](#)]
30. Weißhar, B.; Bessler, W.G. Model-based lifetime prediction of an LFP/graphite lithium-ion battery in a stationary photovoltaic battery system. *J. Energy Storage* **2017**, *14*, 179–191. [[CrossRef](#)]
31. Uddin, K.; Moore, A.D.; Barai, A.; Marco, J. The effects of high frequency current ripple on electric vehicle battery performance. *Appl. Energy* **2016**, *178*, 142–154. [[CrossRef](#)]
32. Korth Pereira Ferraz, P.; Kowal, J. A Comparative Study on the Influence of DC/DC-Converter Induced High Frequency Current Ripple on Lithium-Ion Batteries. *Sustainability* **2019**, *11*, 6050. [[CrossRef](#)]
33. De Breucker, S.; Engelen, K.; D’hulst, R.; Driesen, J. Impact of current ripple on Li-ion battery ageing. *World Electr. Veh. J.* **2013**, *6*, 532–540. [[CrossRef](#)]
34. Beh, H.Z.Z.; Covic, G.A.; Boys, J.T. Effects of pulse and DC charging on lithium iron phosphate (LiFePO<sub>4</sub>) batteries. In *Proceedings of the 2013 IEEE Energy Conversion Congress and Exposition, Denver, CO, USA, 15–19 September 2013*; pp. 315–320. [[CrossRef](#)]
35. Bessman, A.; Soares, R.; Wallmark, O.; Svens, P.; Lindbergh, G. Aging effects of AC harmonics on lithium-ion cells. *J. Energy Storage* **2019**, *21*, 741–749. [[CrossRef](#)]
36. Steinstraeter, M.; Gandlgruber, J.; Everken, J.; Lienkamp, M. Influence of pulse width modulated auxiliary consumers on battery aging in electric vehicles. *J. Energy Storage* **2022**, *48*, 104009. [[CrossRef](#)]
37. Safari, M.; Delacourt, C. Aging of a Commercial Graphite/LiFePO<sub>4</sub> Cell. *J. Electrochem. Soc.* **2011**, *158*, A1123. [[CrossRef](#)]

38. Grolleau, S.; Delaille, A.; Gualous, H.; Gyan, P.; Revel, R.; Bernard, J.; Redondo-Iglesias, E.; Peter, J. Calendar aging of commercial graphite/LiFePO<sub>4</sub> cell—Predicting capacity fade under time dependent storage conditions. *J. Power Source* **2014**, *255*, 450–458. [[CrossRef](#)]
39. Naumann, M.; Spingler, F.B.; Jossen, A. Analysis and modeling of cycle aging of a commercial LiFePO<sub>4</sub>/graphite cell. *J. Power Source* **2020**, *451*, 227666. [[CrossRef](#)]